Enhancing Energy Efficiency through Predictive and Direct Torque Control: An Experimental Study on Induction Motor Drives

***Rozana Alik., Nik Rumzi Nik Idris., Norjulia Mohamad Nordin., Siti Mahfuza Saimon**

Faculty of Electrical Engineering, Universiti Teknologi Malaysia, 81310 Skudai, Johor

***Corresponding Author**

DOI: https://dx.doi.org/10.47772/IJRISS.2025.910000635

Received: 13 October 2025; Accepted: 30 October 2025; Published: 20 November 2025

ABSTRACT

This study presents an experimental comparison between Direct Torque Control (DTC) and Finite Control Set–Predictive Torque Control (FCS-PTC) for a three-phase induction motor (IM) drive, emphasizing their implications for energy efficiency and sustainable industrial operation. Both control methods aim to regulate torque and stator flux yet differ in voltage-vector (VV) selection principles. DTC employs a fixed look-up table with hysteresis controllers, while FCS-PTC evaluates all inverter states through a cost-function-based prediction. Experimental implementation using a dSPACE DS1104 platform was carried out at three operating speeds—286 r/min, 764 r/min, and 1432 r/min—to quantify torque and flux ripples using statistical analysis. At low speed (286 r/min), FCS-PTC achieved a torque ripple of 0.0948 N·m and a flux ripple of 0.0072 Wb, compared with DTC's 0.2350 N·m and 0.0109 Wb. Similar improvements were observed at medium and high speeds, confirming FCS-PTC's superior ability to minimize electromagnetic ripple. Voltage-vector analysis revealed that DTC's avoidance of radial vectors contributes to higher flux variation, whereas FCS-PTC's balanced use of tangential and radial vectors yields smoother electromagnetic response and improved control accuracy. From a societal perspective, the enhanced efficiency of FCS-PTC supports reduced energy consumption and carbon emissions in motor-driven systems, directly aligning with Sustainable Development Goal 7 (Affordable and Clean Energy). The experimental framework also provides a practical platform for engineering education and workforce training in advanced control methods. The findings demonstrate that predictive torque control not only improves technical performance but also contributes to broader objectives of sustainable industrial development and capacity building.

Keywords: Predictive Torque Control (PTC); Direct Torque Control (DTC); Induction Motor Drives; Energy Efficiency; Sustainable Technology

INTRODUCTION

Induction motors (IMs) are the backbone of modern industry. It drives nearly half of global electrical energy consumption in applications ranging from manufacturing and transportation to healthcare and household systems. Their widespread use highlights both their economic significance and their potential role in achieving global energy sustainability. Enhancing the efficiency and stability of IM operation therefore holds strong societal implication, such as reduced energy consumption translates directly into lower carbon emissions, operational costs, and environmental impact.

Achieving precise control of torque and stator flux, however, remains a major challenge, particularly under dynamic operating conditions. A key factor influencing performance is the selection of voltage vectors (VVs), which determines how the control algorithm regulates electromagnetic torque and flux trajectory [1, 2].

Among various strategies, Direct Torque Control (DTC) has been widely adopted for its simple structure and fast dynamic response [3]. Introduced in the 1980s, DTC eliminates the need for current regulators and pulse width modulation by employing hysteresis comparators and a look-up table to determine the appropriate VV based on instantaneous torque and flux errors [4]. Despite these advantages, DTC is often criticized for high

torque and flux ripple, variable switching frequency, and reduced performance near sector boundaries due to limited vector selection options [5-8].

To address these limitations, Predictive Torque Control (PTC), a variant of Finite Control Set-Model Predictive Control (FCS-MPC), has emerged as a promising alternative [9, 10]. PTC employs a predictive model of the machine and evaluates a cost function at each sampling instant to determine the most suitable VV [11]. Unlike DTC, PTC evaluates all possible switching states in a conventional two-level inverter, thereby offering greater control flexibility and improved resolution [12-14].

Several studies have explored DTC and PTC strategies to enhance torque and flux regulation in IM drives [15-19]. Bindal and Kaur [20] proposed a dynamic fuzzy logic based predictive DTC approach that integrates Gaussian membership functions with the Flower Pollination Algorithm to reduce torque ripple. Their simulation results demonstrated improved control under varying speed conditions and emphasized the importance of optimized VV selection. Wang et al. [21] presented an experimental comparison between DTC and PTC under matched switching frequencies. It highlights the PTC's superior VV evaluation capability and DTC's computational efficiency. The study highlighted PTC's flexibility in VV evaluation through cost functions, while DTC maintained an advantage in computational simplicity. Krupa and Koraddi [22] applied PTC in the context of electric vehicle applications, demonstrating that the approach can maintain accurate torque control even under load disturbances and parameter variations using a simulation platform. Xu et al. [23] introduced a hybrid control method combining principles from DTC and Model Predictive Flux Control to reduce torque ripple in switched reluctance motors, with experimental validation confirming improvements in ripple suppression and dynamic robustness.

These studies confirm the benefits of predictive control methods and intelligent VV selection. However, most existing work focuses on performance indicators such as ripple reduction and transient response, with limited emphasis on how VVs are selected and transitioned in real time. Karlovsky and Lettl [24] analyzed switching patterns in both methods and showed PTC's preference for more suitable vectors, but sector-wise VV dynamics across diverse conditions remain insufficiently explored.

This paper builds upon these studies by experimentally analyzing VV selection and sector transitions in DTC and Finite Control Set–Predictive Torque Control (FCS-PTC) for induction motor drives using a dSPACE DS1104 platform. Beyond performance comparison, this study emphasizes the energy-efficiency and educational value of predictive motor control. The experimental framework provides a replicable model for training engineering students and practitioners in sustainable control design, supporting both academic capacity building and industrial innovation. By linking technical advancement with societal goals, the research contributes to the broader pursuit of cleaner, smarter, and more sustainable electrical drive systems.

Modelling of Two-Level Inverter Fed Induction Motor Drive

To investigate and compare the VV selection mechanisms in DTC and FCS-PTC, a mathematical model of the two-level voltage source inverter (VSI) fed IM is established in the stationary reference frame. This model forms the theoretical foundation for analysing VV behaviour and is validated through experimental testing using a dSPACE-controlled inverter-fed IM system.

Induction Motor Model

The stator and rotor voltage equations in the stationary $\alpha - \beta$ reference frame is expressed as:

$$v_s = R_s \cdot i_s + d\psi_s/dt \quad (1)$$

$$v_r = R_r * i_r + d(\psi_r)/dt - j * \omega_r * \psi_r \quad (2)$$

The stator and rotor flux linkages are defined by:

$$\psi_s = L_s * i_s + L_m * i_r \quad (3)$$

$$\psi_r = L_r * i_r + L_m * i_s \quad (4)$$

The electromagnetic torque is computed as:

$$T_e = (3/2) * P * Im(\psi_s * conj(i_s)) \quad (5)$$

where:

- v_s, v_r are the stator and rotor voltage vectors
- i_s, i_r are the stator and rotor current vectors
- ψ_s, ψ_r are the stator and rotor flux linkage vectors
- R_s, R_r are the stator and rotor resistances
- L_s, L_r are the stator and rotor inductances
- L_m is the magnetizing inductance
- P is the number of pole pairs
- ω_r is the rotor electrical angular speed
- $Im()$ and $conj()$ denote the imaginary part and complex conjugate, respectively

The mechanical dynamics of the motor are described by:

$$J * (d\omega_m/dt) = T_e - T_l - B * \omega_m \quad (5)$$

where ω_m is the rotor mechanical speed, J is the moment of inertia, B is the friction coefficient and T_l is the load torque

Two-Level Voltage Source Inverter

The two-level VSI provides eight possible switching states, comprising six active VVs and two zero vectors. These vectors form a regular hexagon in the complex $\alpha - \beta$ plane. Fig. 1 illustrates their geometric arrangement. The six active vectors (v_1 to v_6) are spaced at 60° intervals, while the two zero vectors (v_0 and v_7) lie at the origin. These vectors form the basis for stator flux control in DTC and FCS-PTC strategies. It enables the inverter to regulate torque and flux directly.

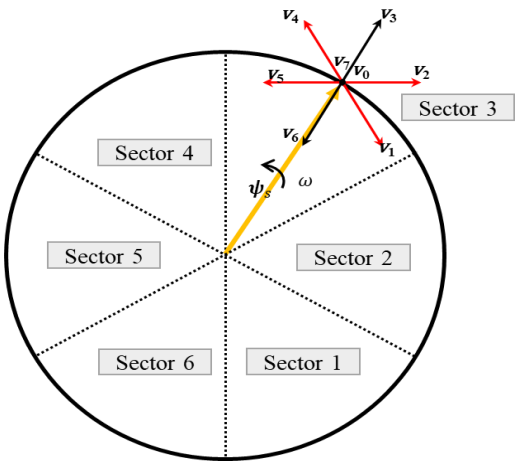

Fig 1. Voltage vector positions and stator flux orientation in the α–β plane

The effect of each VV depends on its orientation relative to the stator flux vector. Referring to Fig. 1, when the flux vector is located in Sector 3, v_3 and v_6 are considered radial vectors and are effective in increasing or decreasing the flux magnitude. Meanwhile, v_4 and v_5, are tangential to the flux trajectory and serve as forward tangential vectors, contributing primarily to torque production. In contrast, v_1 and v_2 act as reverse tangential vectors, reducing torque or changing its direction depending on the control objective [25, 26]. The remaining two vectors, v_0 and v_7, are zero vectors that cause minimal flux change and whose torque influence increases with rotor speed, as shown in (6) [27].

$$\frac{dT_e}{dt} = -\frac{T_e}{\sigma\tau_s} + \frac{1}{\sigma\tau_r} - \frac{3}{2}p^2\frac{L_m}{\sigma L_s L_r}(j\omega_r\psi_s)\Delta j\psi_r \quad (6)$$

where σ is the leakage factor, τ_s and τ_r are the stator and rotor time constants, and ψ_r is the rotor flux linkage

Each switching state corresponds to a unique combination of ON/OFF positions for the inverter legs ($S_A, S_B, S_C \in 0,1$). The output phase voltages relative to the negative DC bus are given by:

$$v_A = (2 * S_A - S_B - S_C) * (V_{dc}/3) \quad (7)$$

$$v_B = (2 * S_B - S_A - S_C) * (V_{dc}/3) \quad (8)$$

$$v_C = (2 * S_C - S_A - S_B) * (V_{dc}/3) \quad (9)$$

The corresponding stator voltage vector in the complex $\alpha - \beta$ plane is:

$$v_s = (2/3) * V_{dc} * \left[(S_A - 0.5 * S_B - 0.5 * S_C) + j * \left(\sqrt{3}/2\right) * (S_B - S_C)\right] \quad (10)$$

where $V_{dc} = 310V$ is the applied DC bus voltage.

Motor and Drive Parameters

The experimental setup consists of a low-power squirrel-cage IM driven by a two-level VSI. The relevant motor electrical and mechanical parameters are summarized in Table 1.

Table 1 Induction motor and drive system parameters used in the experimental setup

Parameter	**Value**
Rated Power	186 W
Rated Speed	1432 r/min
Rated Torque	1 N.m
Line Voltage	190 V
Rated Current	1.4 A
Number of Pole Pairs	2
Stator Resistance (R_s)	9.9 Ω
Rotor Resistance (R_r)	8.15 Ω
Stator Inductance (L_s)	278.6 mH

Rotor Inductance (L_r)	285.3 mH
Magnetizing Inductance (L_m)	265.1 mH
Moment of Inertia (J)	0.001118 kg·m²
Friction Coefficient (B)	0.0006076 N·m·s
Rated Flux (Ψ)	0.32 Wb

Control Algorithms

The control strategies implemented in this work are DTC and FCS-PTC. It operates on fundamentally different principles despite sharing the same inverter-fed IM platform. Both approaches regulate the electromagnetic torque and stator flux by manipulating the inverter switching states, yet they differ significantly in terms of control structure, switching logic, and VV selection methodology.

Direct Torque Control (DTC)

In this study, the DTC method was implemented to regulate the stator flux and electromagnetic torque of the IM by selecting optimal VVs based on instantaneous flux and torque errors. As shown in Fig. 2, the control structure relies on three main stages: (i) flux and torque estimation, (ii) sector identification, and (iii) VV selection using a predefined look-up table (LUT). The detailed implementation is described below.

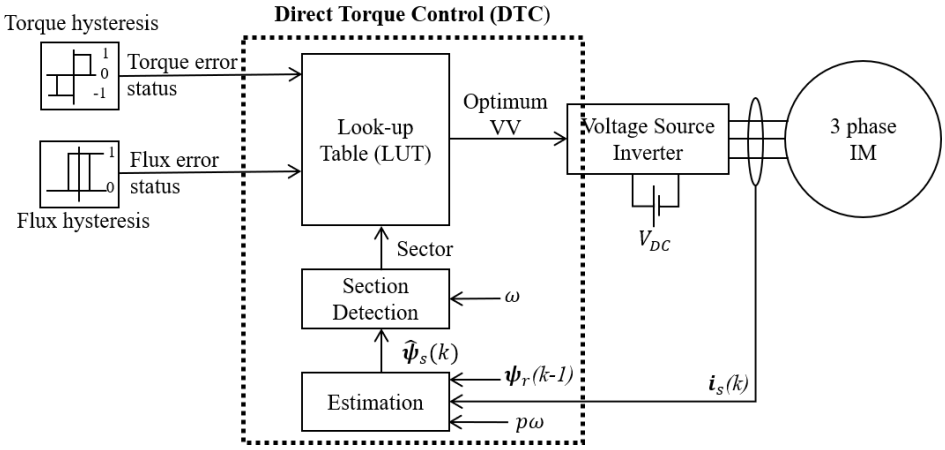

Fig. 2 Block diagram of the conventional Direct Torque Control (DTC) scheme

(i) Flux and Torque Estimation

The stator flux vector $\boldsymbol{\psi_s}$ is estimated using the following relation in the stationary α–β reference frame:

$$\boldsymbol{\psi_s} = \int (\boldsymbol{v_s} - R_s * \boldsymbol{i_s}) dt \quad (11)$$

where v_s is the stator voltage vector, R_s is the stator resistance, and i_s is the stator current vector. The magnitude and angle of the stator flux vector are then computed as:

$$|\boldsymbol{\psi_s}| = \sqrt{(\psi_\alpha^2 + \psi_\beta^2)} \quad (12)$$

$$\theta_{\psi_s} = \arctan(\psi_\beta / \psi_\alpha) \quad (13)$$

The electromagnetic torque is computed as:

$$T_e = (3/2) * p * (\psi_\alpha * i_\beta - \psi_\beta * i_\alpha) \quad (14)$$

where p is the number of pole pairs.

(ii) Sector Identification

The α–β plane is divided into six sectors of 60° each. The calculated angle θ_{ψ_s} in Eqn (13) determines which sector the $\boldsymbol{\psi}_s$ is currently located in. This information is used to guide the VV selection.

(iii) Voltage Vector Selection via LUT

The instantaneous torque and flux errors are compared against hysteresis bands to generate discrete outputs. The torque error is processed using a three-level hysteresis comparator with a bandwidth of ±0.2 N.m, producing outputs of +1, 0, or –1. The flux error is processed using a two-level comparator with a bandwidth of ±0.01 Wb, producing outputs of +1 or –1. These outputs, along with the identified flux sector, determine the appropriate VV to apply via a predefined look-up table (Table 2) [28, 29].

Table 2 Conventional Look-up Table (LUT)

Flux Error	Torque Error	Sector 1	Sector 2	Sector 3	Sector 4	Sector 5	Sector 6
1	1	V_2	V_3	V_4	V_5	V_6	V_1
1	0	V_0	V_7	V_0	V_7	V_0	V_7
1	-1	V_6	V_1	V_2	V_3	V_4	V_5
0	1	V_3	V_4	V_5	V_6	V_1	V_2
0	0	V_7	V_0	V_7	V_0	V_7	V_0
0	-1	V_5	V_6	V_1	V_2	V_3	V_4

Finite Control Set–Predictive Torque Control (FCS-PTC)

This work employs a Finite Control Set–Predictive Torque Control (FCS-PTC) strategy to regulate the torque and stator flux of the IM. At every sampling instant, the algorithm evaluates a predefined set of inverters VVs and selects the optimal one by minimizing a cost function.

The FCS-PTC process involves three main steps: (i) estimation of torque and stator flux, (ii) prediction of future states using a discrete-time model, and (iii) VV selection via cost function minimization. Fig. 3 shows the block diagram of the implemented FCS-PTC scheme.

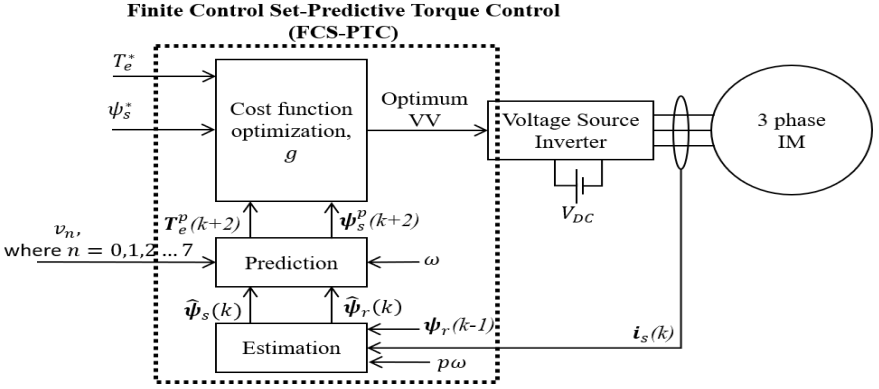

Fig. 3 Block diagram of the Predictive Torque Control (PTC) scheme

The stator flux and torque estimations are based on the same expressions used in the DTC method (refer to equations (11) and (14)). These estimates serve as inputs to the prediction model, which predicts the stator flux at the next control interval using:

$$\psi\square(k+1) = \psi\square(k) + T\square \cdot \left(v\square(k) - R\square \cdot i\square(k)\right) \quad (15)$$

where $\psi\square(k)$ is the estimated stator flux at the current step, $T\square$ is the sampling period (40 µs), $v\square(k)$ is the applied VV, $R\square$ is the stator resistance, and $i\square(k)$ is the measured stator current vector.

The torque is predicted using:

$$T_{\mathrm{e}} = (3/2) \cdot P \cdot Im\psi\square \cdot i_s^* \quad (16)$$

where P is the number of pole pairs, $Im\{\cdot\}$ denotes the imaginary component, and i_s^* is the complex conjugate of the stator current vector

Once the predictions for all VVs are computed, a cost function is used to determine the most suitable VV. The cost function employed in this work is given by:

$$g = \left|T_e^* - T_e^p\right| + \lambda \cdot \left|\psi_s^* - \psi_s^p\right| \quad (17)$$

where T_e^* and ψ_s^* are the reference torque and stator flux magnitude, T_e^p and ψ_s^p are the predicted values for each VV, and λ is the weighting factor. VV that minimizes the cost function is selected and applied in the next interval. This process is repeated at every sampling cycle.

Experimental Test Conditions

To evaluate and compare the performance of the DTC and FCS-PTC strategies, a series of experiments were conducted under varying speed conditions. The IM was tested at three distinct speeds representing low, medium, and high operating conditions: 286 r/min (20% of rated speed), 764 r/min (approximately 57% of rated speed), and 1432 r/min (rated speed). No external mechanical load was connected to the motor shaft. The motor operated solely against its internal frictional torque. This condition allows for a clearer assessment of control performance without interference from load dynamics. Additionally, since the VV selection logic in DTC and FCS-PTC is not influenced by load torque, the no-load condition provides a valid basis for comparison. The complete laboratory setup is illustrated in Fig. 4.

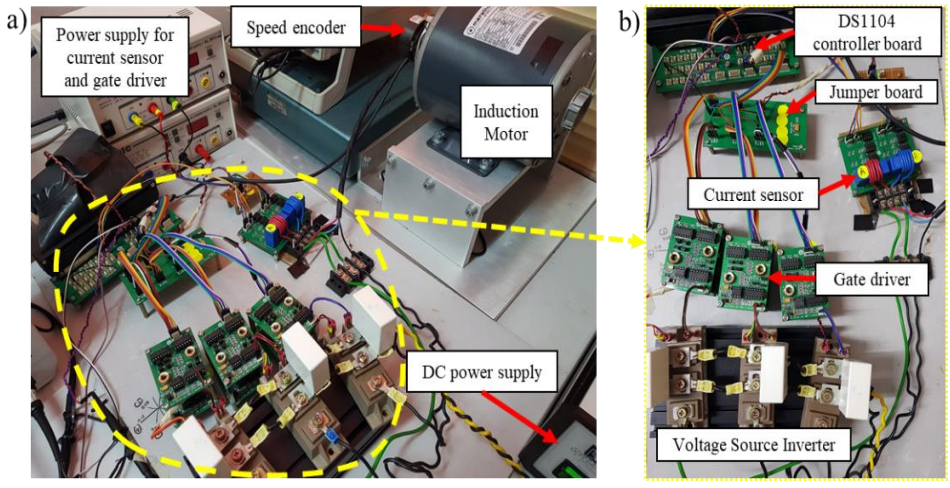

Fig. 4 Experimental setup for real-time implementation of DTC and FCS-PTC using a two-level VSI and a dSPACE DS1104 controller

The experiments were carried out on a three-phase squirrel-cage IM (186 W, 1425 r/min, 50 Hz, 190 V, 1.4 A, 2 pole pairs). The drive was supplied by a two-level VSI using Fuji Electric IGBT modules (rated 1200 V, 100

A) with 0.47 μF / 1600 V snubber capacitors for over-voltage protection. A dSPACE DS1104 controller board executed the algorithms in real time, programmed in C, with a sampling time of 40 μs and an inverter switching frequency of 20 kHz. The DS1104 provides 12-bit/16-bit ADCs (±10 V range) for signal acquisition and 16-bit DACs (±10 V range) for analogue outputs, ensuring accurate and reproducible control implementation.

Motor currents were measured with Hall-effect current sensors (±50 A range, powered by ±12.5 V supply) calibrated via a short-circuit test. Each sensor employed five conductor turns on the magnetic core to improve sensitivity, with a gain of 9 V/A, yielding reliable measurements within ±2% accuracy. Speed was measured by an incremental optical encoder (2048 pulses/rev, TTL/RS422 compatible) sampled at 1 ms intervals, ensuring precise tracking of rotor position and speed. The inverter switching was driven through a dedicated gate driver board (5 V to 15 V signal amplification) with a blanking time of 3 μs to prevent shoot-through. Connections between controller and gate drivers were organised via a jumper board for stable interfacing. A regulated DC power supply provided ±12.5 V for sensors and auxiliaries.

During each test, the electromagnetic torque, stator flux, and applied VV signals were monitored via the DS1104 DAC channels and Hall-effect current sensors, routed to a Rohde & Schwarz digital oscilloscope through shielded BNC cables to minimise noise. The oscilloscope traces were saved in CSV format and transferred to a PC via USB. The files were then imported into MATLAB using the readtable function for post-processing. In MATLAB, torque and flux ripples were quantified by calculating the standard deviation of their time-domain waveforms. VV switching behaviour was extracted by threshold-based classification of the DAC outputs corresponding to the applied VVs. The resulting discrete labels were subsequently counted over the full observation window to determine the occurrence frequency of each VV. This post-processing step was necessary because MATLAB provided precise tools for signal filtering, numerical evaluation, and statistical analysis (e.g., standard deviation for ripple quantification). Direct oscilloscope measurement alone could not ensure the same level of repeatability or allow synchronized comparison across operating points. Hence, the extraction and MATLAB-based analysis ensured a fair and transparent evaluation of DTC and FCS-PTC performance. The evaluation focused on three key performance indicators: torque ripple, stator flux variation, and VV switching behaviour.

Prior to the comparative tests, both controllers were tuned to ensure a fair, near-optimal operating point for our setup. For DTC, flux and torque hysteresis widths were swept within practical bounds reported in the literature (flux: 0.005–0.02 Wb; torque: 0.1–0.3 N·m) [30, 31] and evaluated at 764 r/min (medium speed) to balance flux/ torque ripple and switching activity. The selected ±0.01 Wb (flux) and ±0.2 N·m (torque) produced low ripple without excessive switching. For FCS-PTC, the weighting factor, λ in the equation (17) was varied over a broad range (e.g., 5–50). The chosen λ =30 consistently yielded lower flux ripple with no degradation in torque tracking across all three speeds in the rig, while smaller λ increased flux variation and larger λ produced marginal benefits at the cost of more aggressive switching. These settings were then fixed for all experiments to preserve comparability.

Although all experiments were conducted under no-load, steady-state conditions, this setup was intentionally selected to isolate the intrinsic control behaviors of DTC and FCS-PTC without external mechanical interference. Such conditions allow a fair assessment of the voltage-vector selection mechanism and its direct impact on torque and flux regulation. Nonetheless, this configuration does not capture the dynamic responses or efficiency variations that occur under real industrial load conditions. Future extensions of this study will incorporate mechanical loading and transient profiles (acceleration, deceleration, and regenerative braking) to assess the controllers' adaptability and robustness in practical operating environments.

RESULTS AND DISCUSSION

This section presents a comparative analysis of the DTC and FCS-PTC strategies under varying speed conditions: 286 r/min (low), 764 r/min (medium), and 1432 r/min (high). The performance metrics evaluated include torque ripple, stator flux variation, and VV selection patterns. Data were obtained from real-time experiments using the dSPACE DS1104 controller.

Torque and Flux Ripple Analysis

Representative raw oscilloscope traces for DTC and FCS-PTC at three operating speeds (≈286, 764, and 1432 r/min) are shown in Figs. 5 and 6. These captures document the experimental nature of the study and illustrate the unprocessed signals obtained during steady-state operation. The traces include measured speed, phase current, estimated torque, and stator flux waveforms. However, the detailed analysis in this work focuses primarily on torque and flux behaviour, while the current and speed waveforms are shown only for completeness.

To enable a clear performance comparison, the corresponding oscilloscope data were exported as CSV and processed in MATLAB. Fig. 7 shows the resulting torque and flux waveforms (aligned and scaled), and Table 3 summarises both the standard deviation values (ripple metric) and the Integral of Absolute Error (IAE, tracking accuracy metric) [32, 33]. The Integral of Absolute Error (IAE) was computed over a fixed steady-state window T = 1 s, as

$$IAE = \int_{t_0}^{T} |e(t)|\, dt \qquad \left(discrete\ form: \sum_{k=1}^{N} |e[k]| \Delta t \right), \qquad (18)$$

where e is the torque or flux error, and Δt is the oscilloscope sampling interval used for the CSV export.

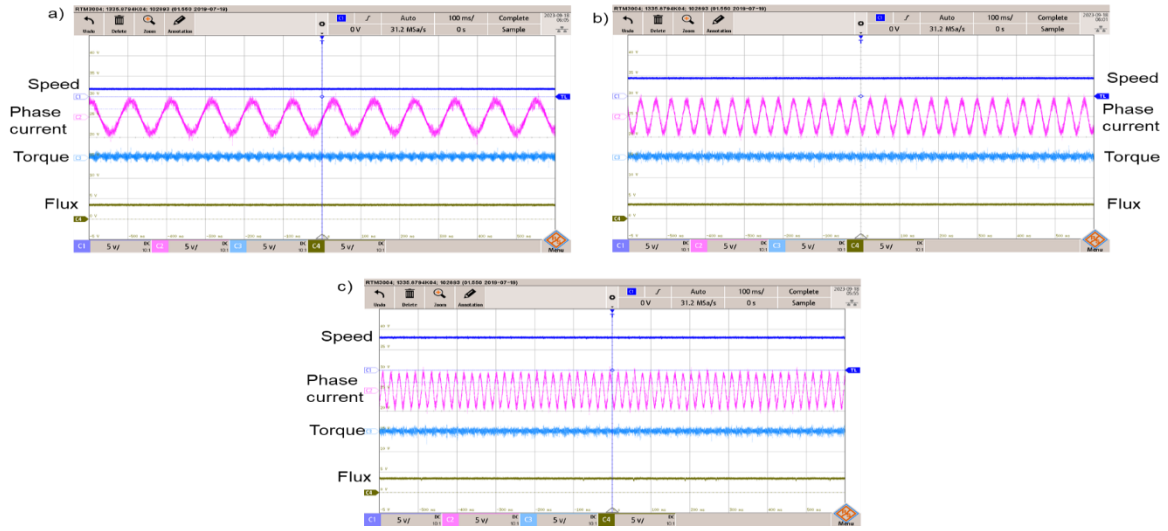

Fig. 5 Oscilloscope traces for DTC at three operating speeds: a) 286 r/min, b) 764 r/min, and c) 1432 r/min

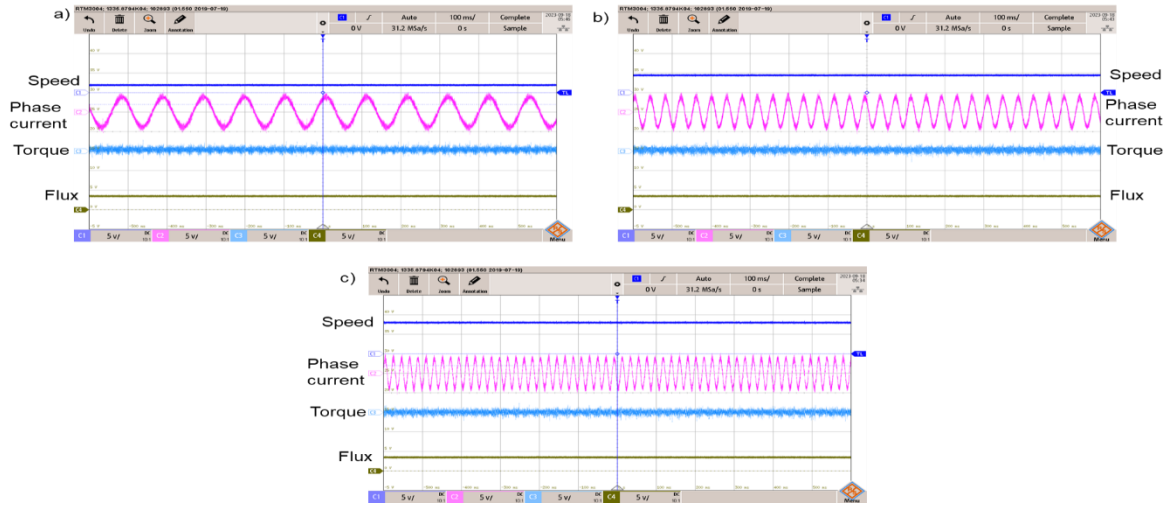

Fig. 6 Oscilloscope traces for FCS-PTC at three operating speeds: a) 286 r/min, b) 764 r/min, and c) 1432 r/min

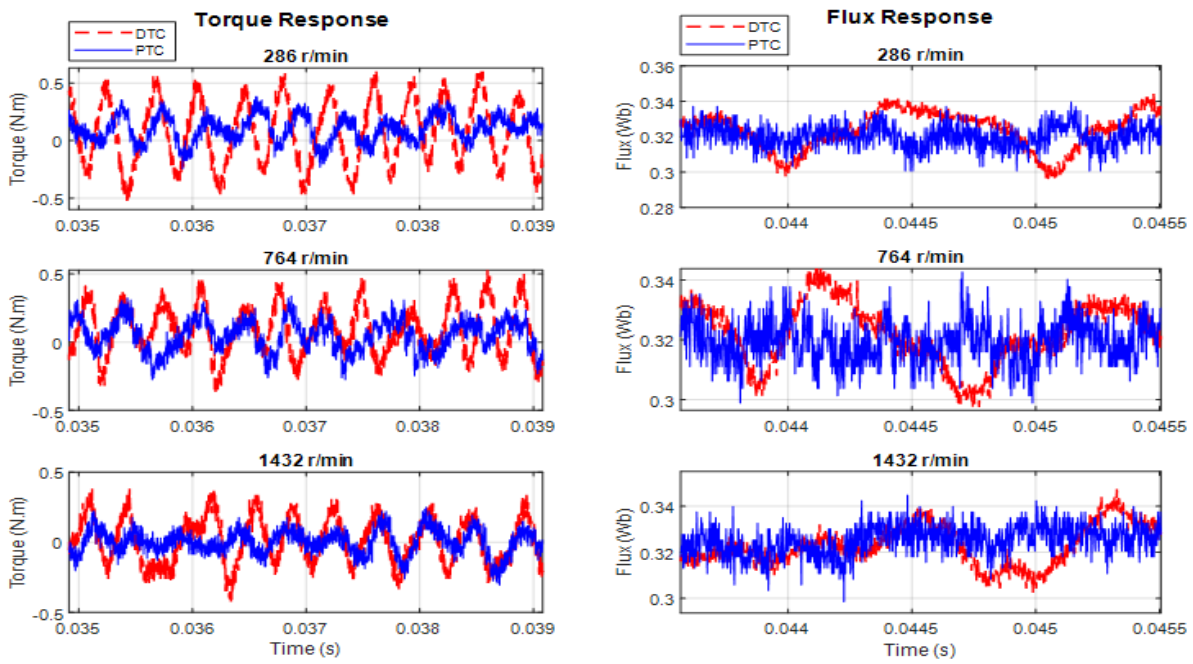

Fig 7. Comparison of Torque and Flux Response

Table 3 Standard deviation of torque and flux for DTC and FCS-PTC at different speeds

Speed (r/min)	Method	Torque Std. Dev (N.m)	Flux Std. Dev (Wb)	Torque IAE (N.m.s)	Flux IAE (Wb.s)
286	DTC	0.234982	0.010884	0.018622	0.00017766
	FCS-PTC	0.094766	0.007244	0.018241	0.00011453
764	DTC	0.187628	0.010560	0.018545	0.00017769
	FCS-PTC	0.111990	0.006940	0.018942	0.00011107
1432	DTC	0.190512	0.011200	0.020044	0.00018575
	FCS-PTC	0.081327	0.008611	0.019904	0.00016410

As seen from the data, FCS-PTC consistently demonstrates lower torque ripple and improved flux stability compared to DTC across all speed conditions. During low speed (286 r/min), the torque ripple under DTC is 0.234982 N.m, more than double the ripple under FCS-PTC (0.094766 N.m). Flux ripple is also significantly larger in DTC, indicating that hysteresis-based switching leads to frequent and abrupt VV changes. These effects are amplified at low speeds due to weak back-EMF and less damping.

At medium speed (764 r/min), DTC torque ripple slightly reduces but remains higher than FCS-PTC. The FCS-PTC maintains better flux control, with a flux standard deviation of 0.006940 Wb. This suggests that FCS-PTC enables smoother VV transitions and more stable flux behaviours during steady-state operation. At high speed (1432 r/min), the torque ripple in DTC remains roughly constant, but FCS-PTC achieves further reduction. This shows that FCS-PTC adapts better at higher speeds, where the flux estimation becomes more sensitive to current sensor noise and inverter non-linearity. The ability to predict and evaluate all VVs at each sampling point improves its dynamic response.

In addition to ripple, the IAE values confirm that FCS-PTC achieves comparable or slightly improved tracking accuracy relative to DTC. For torque, the IAE values are very close between both methods (e.g., 0.01824 vs 0.01862 at 286 r/min), indicating that the ripple reduction achieved by FCS-PTC does not compromise steady-

state accuracy. Flux IAE, however, shows a clearer advantage for FCS-PTC (0.000111 vs 0.000178 at 764 r/min), reinforcing its ability to maintain tighter flux regulation.

The observed reduction in torque and flux ripples with FCS-PTC is a consequence of its cost function–based VV selection. Unlike DTC, which depends on fixed hysteresis bands and a predefined LUT, FCS-PTC evaluates all candidate VVs at each sampling interval and selects the one that best minimizes the predicted torque and flux errors. This results in smoother torque production and improved flux stability. To further understand the switching behaviours and control effectiveness, the next section examines the VV occurrence and sector distribution patterns observed during experimentation.

It is worth noting that the analysis of energy efficiency in this work is inferred indirectly through reduced torque and flux ripples. Lower ripple corresponds to diminished copper and iron losses, thereby suggesting improved electromagnetic efficiency. However, since no direct electrical input versus mechanical output power measurement was performed, the reported "efficiency improvement" reflects the control system's potential rather than absolute efficiency values. Future tests with integrated power analyzers will enable empirical verification of this relationship.

Voltage Vector and Sector Distribution Analysis

As introduced in Section 2.2, the stator flux plane in DTC and FCS-PTC is divided into six equal sectors. However, for the purpose of detailed VV analysis, this study focuses on Sector 3. This is justified since the switching behaviours are cyclic across sectors, and observations in Sector 3 are representative of general behaviours. Only seven VVs (v_0 to v_6) are considered in this analysis. Although the inverter supports eight possible vectors, v_0 and v_7 are both zero vectors and produce the same electromagnetic effect. Therefore, to simplify implementation and interpretation, only v_0 is used to represent the zero vector in both DTC and FCS-PTC strategies.

Since DTC employs a fixed look-up table with deterministic switching, its VV time traces are not shown here. Instead, representative switching plots (sector, selected VV, torque, and flux) are provided only for FCS-PTC, where adaptive cost-function-based selection produces more informative behaviours. Fig. 8 illustrates the selected sector number (dark blue) and VV number (pink) versus time, together with torque and flux responses, for FCS-PTC at three speeds. Fig. 9 summarises the occurrence counts of each VV in Sector 3 for both DTC and FCS-PTC, enabling a direct comparison of switching diversity across methods.

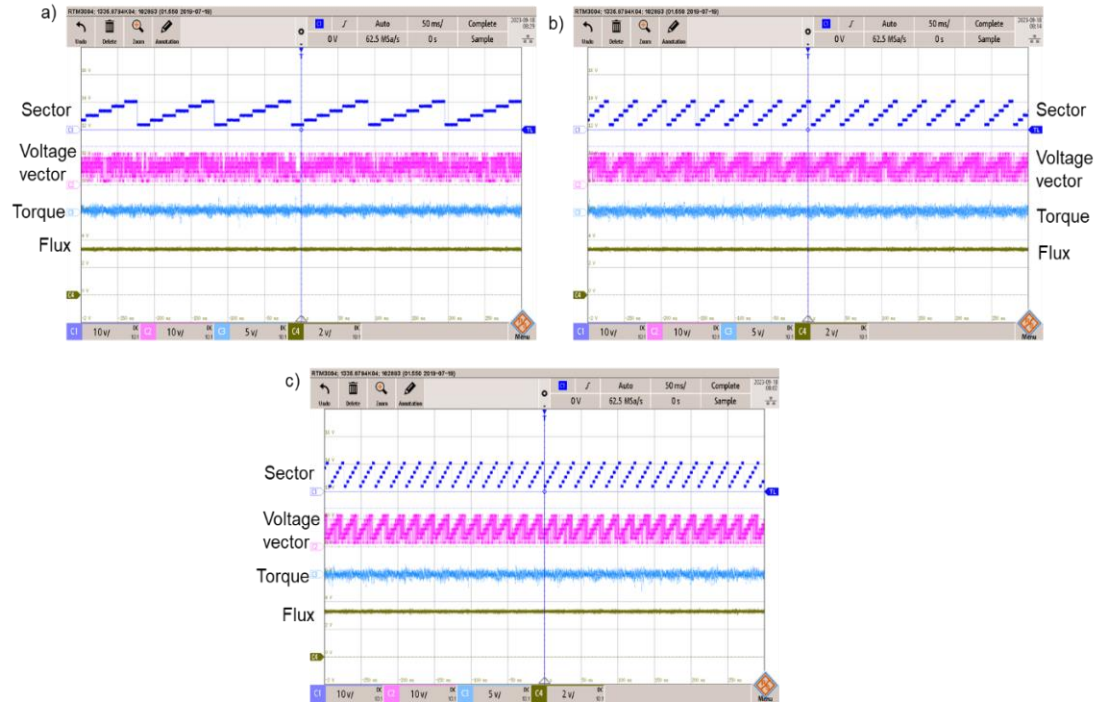

Fig. 8. VV trace for FCS-PTC at three different speeds: a) 286 r/min, b) 764 r/min, and 1432 r/min

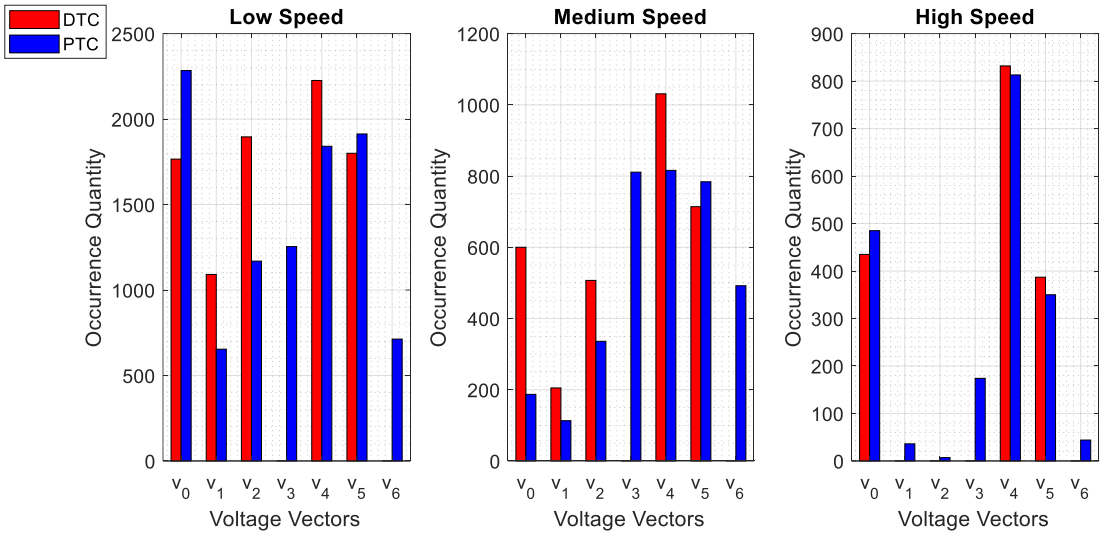

Fig. 9. Occurrence quantity of voltage vectors at Sector 3

At low speed (286 r/min), Fig. 9 shows that DTC relies heavily on the v_0. This behaviour tends to reduce the stator flux amplitude over time, a phenomenon commonly referred to as flux droop. Since radial VVs (such as v_3 and v_6) are not applied in DTC, the flux control becomes dependent solely on v_0, making DTC ineffective in restoring flux amplitude. This explains the higher flux ripple observed under DTC in Section 3.1. The omission of v_3 and v_6 can also be confirmed directly from the DTC LUT (Table 2): for every sector, the LUT only maps flux and torque hysteresis states to tangential or zero vectors, and never assigns radial vectors. This confirms that their absence in the experimental results is not incidental but a fundamental feature of the DTC switching logic. Furthermore, Fig. 10 illustrates the theoretical influence of radial vectors v_3 and v_6 on the stator flux magnitude and torque, explaining why they are excluded from the DTC switching table but selectively included by FCS-PTC.

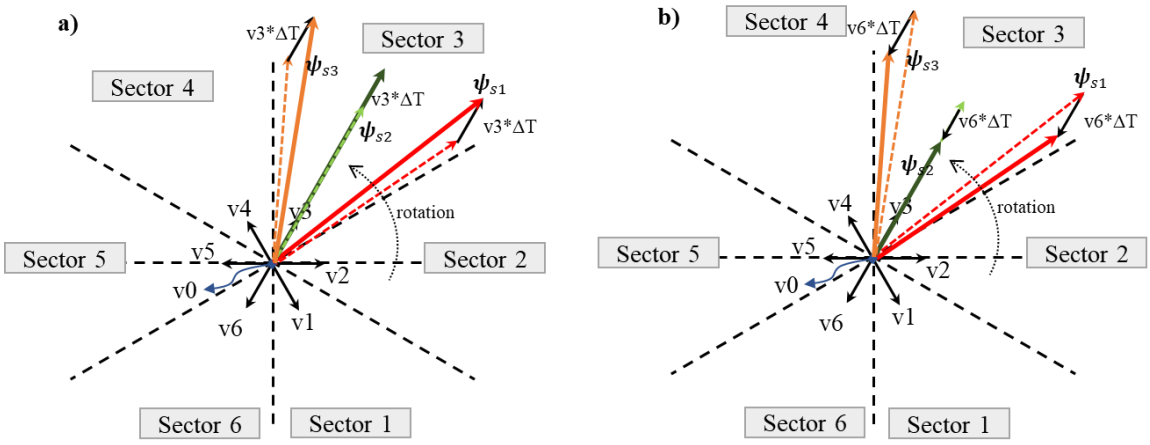

Fig. 10. Voltage vector effect in Sector 3 according to three flux vector positions:

a) Application of v_3 and b) Application of v_6

When the flux vector is positioned at the beginning of the sector (denoted as ψ_{s1}, red arrow), applying v_3 rapidly increases the flux magnitude while causing a slow increase in torque. At the middle position (ψ_{s2}, green arrow), v_3 still causes a rapid flux rise but induces no torque change. At the end of the sector (ψ_{s3}, orange arrow), v_3 again increases flux but results in a slow torque decrease. The behaviours of v_6, which is the radial VV opposite to v_3, mirrors these effects. It causes a consistent reduction in flux magnitude, with similar torque changes depending on the vector's position. The significant influence of v_3 and v_6 on flux makes them difficult to control using the conventional hysteresis-based DTC, hence their exclusion from the DTC

switching table. However, this omission leads to over-reliance on v_0 for flux regulation, often resulting in flux droop and high ripple, especially under low-speed conditions. Conversely, Figs. 8 and 9 demonstrate that FCS-PTC does not limit VV selection. It optimally includes radial vectors when needed to dynamically balance both torque and flux, enabling finer control and lower ripple under varying operating conditions.

At medium speed (764 r/min), the occurrence results in Fig. 9 indicate that DTC still avoids radial vectors v_3 and v_6, while FCS-PTC makes selective use of them for fine flux control. This ability to engage radial vectors dynamically explains the improved flux stability of FCS-PTC compared to DTC.

At high speed (1432 r/min), DTC shows less application of v_1 and v_2, as seen in Fig. 9, highlighting a limitation in tangential VV diversity. As discussed in Section 2.2, v_1 and v_2 are categorized as forward tangential vectors, which are typically responsible for increasing torque depending on the flux vector position. Their absence implies that torque control relies heavily on repeated application of other tangential vectors such as v_4 and v_5, or even zero vectors, depending on the hysteresis controller's response. This behaviour is likely caused by the aggressive nature of hysteresis control at higher speeds, where the torque error changes rapidly. The hysteresis controller tends to favour vectors that produce stronger, immediate torque responses, leading to neglect of smoother vectors like v_1 and v_2. Consequently, torque transitions become uneven and ripple increases.

Table 4 presents a comparative summary of VV selection characteristics for DTC and FCS-PTC. The table highlights how each method handles VV diversity and its implications on flux and torque control. This overview reinforces the observed performance trends and explains why FCS-PTC delivers superior ripple performance across all speed conditions.

Table 4 Comparison of Voltage Vector Selection between DTC and FCS-PTC

Aspect	**DTC**	**FCS-PTC**
VV Selection Method	Fixed Look-Up Table (LUT) based on flux and torque hysteresis states	Evaluates all 7 active VVs using a cost function at each sampling instant
VV Variety Used	Limited (usually excludes radial VVs)	Full set of VVs
Use of Zero Vector	Frequently selected to control flux, especially at low speed	Selectively applied based on prediction outcome and cost function
Use of Radial VVs	Not used at all	Utilized for fine flux control especially at low and medium speeds
Use of Tangential VVs	Limited to specific pairs depending on sector and LUT logic	All tangential VVs considered and used depending on prediction effectiveness
Impact on Flux Control	Indirect via zero vector and limited tangential options	Direct control via radial vectors and cost-optimized decisions
Impact on Torque Control	Dependent on hysteresis width and LUT choice	Optimized via cost function prioritization

Limitations and future work

This study compared DTC and FCS-PTC under steady-state, no-load conditions to isolate intrinsic control characteristics and ensure reproducibility. While this approach clarifies the direct influence of voltage-vector selection, it does not account for dynamic load interactions, mechanical inertia, or regenerative effects common in industrial environments. Therefore, the findings should be interpreted as baseline control characteristics rather than complete system efficiency data.

Future extensions should consider transient operations such as acceleration, deceleration, and regenerative braking, where voltage-vector transition dynamics may differ significantly. Investigating these regimes would provide deeper insights into energy recovery, drive stability, and adaptability under real-world conditions. Further, integrating multi-objective cost functions that simultaneously optimize energy efficiency, torque smoothness, and switching losses could enhance the relevance of predictive control for industrial sustainability.

From a social and educational perspective, this experimental framework can be expanded into training modules for engineering students and technicians, equipping them with hands-on experience in sustainable motor-drive control. Future work should include variable and transient load testing using a dynamometer setup, enabling evaluation of torque response, efficiency, and thermal performance under realistic operating conditions. Integrating a power analyzer would allow direct measurement of input electrical power and output mechanical torque, providing quantitative validation of energy efficiency claims. Moreover, comparative analysis of computational cost and control delay between FCS-PTC and conventional DTC would help assess practical implementation feasibility in real-time embedded systems. Also, exploring adaptive or multi-objective cost functions could further enhance predictive control accuracy while balancing energy efficiency and switching loss trade-offs. Finally, future collaborations with industry could translate these results into policy recommendations for energy-efficient motor standards, supporting Malaysia's transition toward low-carbon and smart-manufacturing initiatives.

CONCLUSION

This study presented a comparative experimental evaluation of DTC and FCS-PTC for an induction motor drive across varying speed conditions. Results demonstrated that FCS-PTC consistently reduced torque and flux ripples relative to DTC, particularly at low speed where the conventional DTC approach exhibits excessive flux ripple due to limited voltage-vector diversity. Analysis of voltage-vector selection revealed that DTC's fixed look-up table restricts radial and tangential vector utilization, while FCS-PTC's predictive approach evaluates all possible vectors, enabling smoother torque response, improved flux regulation, and enhanced electromagnetic stability.

Beyond technical improvement, these outcomes signify tangible societal benefits. Improved torque control contributes to higher energy efficiency and reduced electrical losses in industrial systems, which supports Sustainable Development Goals (SDGs) related to clean energy and responsible production. The experimental platform also provides a replicable model for experiential learning and workforce training in advanced control systems, strengthening local engineering capacity.

Although the present evaluation was limited to no-load steady-state conditions, the results establish a strong foundation for subsequent energy-efficiency validation under dynamic operating regimes. The consistent ripple reduction achieved by FCS-PTC suggests potential for lower energy losses and smoother drive operation, which warrants future confirmation through direct input–output power analysis.

Overall, the study confirms that predictive torque control not only offers superior dynamic performance but also aligns with broader social objectives of sustainable energy use, technological innovation, and educational advancement. It thus serves as a bridge between engineering research and societal impact, promoting the integration of intelligent control methods into future industrial and academic ecosystems.

REFERENCES

1. Aziz, A.G.M.A., et al., A comprehensive examination of vector-controlled induction motor drive techniques. Energies, 2023. 16(6): p. 2854.
2. Bhowate, A., M. Aware, and S. Sharma, Predictive torque control with online weighting factor computation technique to improve performance of induction motor drive in low speed region. IEEE Access, 2019. 7: p. 42309-42321.
3. Takahashi, I. and T. Noguchi, A new quick-response and high-efficiency control strategy of an induction motor. IEEE Transactions on Industry applications, 1986(5): p. 820-827.

4. Djamila, C. and M. Yahia, Direct torque control strategies of induction machine: comparative studies. Direct Torque Control Strategies of Electrical Machines, 2020: p. 17.
5. Tatte, Y. and M. Aware, Twelve sectors direct torque control for three-level inverter fed induction motor drive. Electrical Engineering, 2024: p. 1-15.
6. Aissa, O., et al., Advanced direct torque control based on neural tree controllers for induction motor drives. ISA transactions, 2024. 148: p. 92-104.
7. Lodi, K.A., et al., Ann-based improved direct torque control of open-end winding induction motor. IEEE Transactions on Industrial Electronics, 2024. 71(10): p. 12030-12040.
8. Cai, J., et al., Overview of the direct torque control strategy in switched reluctance motor drives. IEEE Transactions on Transportation Electrification, 2024. 11(1): p. 1617-1628.
9. Rodriguez, J. and P. Cortes, Predictive control of power converters and electrical drives. 2012: John Wiley & Sons.
10. Mukhopadhyay, S., S. Mansani, and S. Sekaran, Torque ripple minimization and speed control of switched reluctance motor employing model predictive controller. Electrical Engineering, 2024. 106(6): p. 7035-7054.
11. Geyer, T., Model predictive control of high power converters and industrial drives. 2016: John Wiley & Sons.
12. Mamdouh, M. and M.A. Abido, Efficient predictive torque control for induction motor drive. IEEE Transactions on Industrial Electronics, 2018. 66(9): p. 6757-6767.
13. Mousavi, M.S., et al., Predictive torque control of induction motor based on a robust integral sliding mode observer. IEEE Transactions on Industrial Electronics, 2022. 70(3): p. 2339-2350.
14. Shahid, M.B., et al., Torque error based auto-tuning of weighting factor in model predictive torque control of induction motor drive. Journal of Electrical Engineering & Technology, 2023. 18(3): p. 1959-1973.
15. Kumar, R.H., A. Iqbal, and N.C. Lenin, Review of recent advancements of direct torque control in induction motor drives–a decade of progress. IET Power Electronics, 2018. 11(1): p. 1-15.
16. El Ouanjli, N., et al., Modern improvement techniques of direct torque control for induction motor drives-a review. Protection and Control of Modern Power Systems, 2019. 4(2): p. 1-12.
17. Mohanraj, D., et al., Critical aspects of electric motor drive controllers and mitigation of torque ripple. IEEe Access, 2022. 10: p. 73635-73674.
18. Bhowate, A., M.V. Aware, and S. Sharma, Predictive torque control algorithm for a five-phase induction motor drive for reduced torque ripple with switching frequency control. IEEE Transactions on Power Electronics, 2019. 35(7): p. 7282-7294.
19. Li, Z., et al., Fault-tolerant predictive torque control design for induction motor drives based on discrete space vector modulation. IEEE Journal of Emerging and Selected Topics in Power Electronics, 2021. 9(5): p. 5441-5451.
20. Bindal, R.K. and I. Kaur, Torque ripple reduction of induction motor using dynamic fuzzy prediction direct torque control. ISA transactions, 2020. 99: p. 322-338.
21. Wang, F., et al., A comprehensive study of direct torque control (DTC) and predictive torque control (PTC) for high performance electrical drives. EPE Journal, 2015. 25(1): p. 12-21.
22. Krupa, T., S. Koraddi, and A. Raju. Model Predictive Torque Control of Induction Motor for Electric Vehicle Application. in 2024 International Conference on Innovation and Novelty in Engineering and Technology (INNOVA). 2024. IEEE.
23. Xu, A., et al., A new control method based on DTC and MPC to reduce torque ripple in SRM. IEEE Access, 2019. 7: p. 68584-68593.
24. Karlovsky, P. and J. Lettl, Induction motor drive direct torque control and predictive torque control comparison based on switching pattern analysis. Energies, 2018. 11(7): p. 1793.
25. Idris, N.R.N. and T. Sutikno. High performance direct torque control of induction motor drives: Problems and improvements. in 2017 4th International Conference on Electrical Engineering, Computer Science and Informatics (EECSI). 2017. IEEE.
26. Casadei, D., et al. Effects of flux and torque hysteresis band amplitude in direct torque control of induction machines. in Proceedings of IECON'94-20th Annual Conference of IEEE Industrial Electronics. 1994. IEEE.

27. Alsofyani, I.M. and N.R.N. Idris, Simple flux regulation for improving state estimation at very low and zero speed of a speed sensorless direct torque control of an induction motor. IEEE Transactions on power electronics, 2015. 31(4): p. 3027-3035.
28. Rahman, M.F. and S.K. Dwivedi, Modeling, simulation and control of electrical drives. Vol. 118. 2019: Institution of Engineering and Technology.
29. Takahashi, I. and Y. Ohmori, High-performance direct torque control of an induction motor. IEEE transactions on industry applications, 1989. 25(2): p. 257-264.
30. Zaky, M.S., H.A. Maksoud, and S.M. Shaban, Analysis of Hysteresis Band Variations in DTC on the Performance of IM Drives. Journal of Electrical Systems, 2020. 16(3).
31. Mathapati, S. and J. Bocker, Analytical and offline approach to select optimal hysteresis bands of DTC for PMSM. IEEE Transactions on Industrial Electronics, 2012. 60(3): p. 885-895.
32. Zellouma, D., et al., Using the rooted tree optimization to increase the performance of the improved backstepping control used to control the induction machine. Measurement and Control, 2025: p. 00202940251340675.
33. Terfia, E.-s., et al., Optimal Fractional Order Proportional Integral Controller for Dual Star Induction Motor Based on Particle Swarm Optimization Algorithm. Journal Européen des Systèmes Automatisés, 2023. 56(2).